# New Approach to Evaluate Joint Delamination Mechanism of Divertor by Finite Element Analysis Applying Cohesive Zone Model (CZM); Parametric Study on the Maximum Traction under Heating

Yuta TOBATA*, Motoki NAKAJIMA, Dai HAMAGUCHI, Takashi NOZAWA

*National Institutes for Quantum Science and Technology (QST), Rokkasho, Aomori 039-3212, Japan*

(Received 9 October 2024 / Accepted 23 December 2024)

To evaluate the delamination mechanism of the joint interfaces of a plasma-facing component, a new approach using the finite element analysis (FEA) applying the cohesive zone model (CZM) is proposed. The parametric study on the maximum traction $\tau_{max}$, which is one of the principal CZM parameters, was conducted for compensating the lack of material data. Monotonic heat loading was applied to the surface up to 20 MW/m$^2$ in 1 second. The traction-separation law was assumed to be bilinear, which represents the relation between the representative crack stress and its opening displacement used for CZM. In the parametric study, three assumptions of $\tau_{max}$ were defined, (1) equal to the weaker bulk strength (Copper), (2) considering temperature dependency, and the average value of the strength ratio of the interface to bulk copper, and (3) considering as well as (2) but the lowest value of the ratio. Results of the parametric study suggest shear stress-governed (mode II) delamination without vertical crack propagation in tungsten monoblock. Meanwhile, the joint interface shows compression, which means the interface remains in contact. Therefore, it is suggested that the degradation of cooling capability does not happen during the heating process unless vertical cracks in tungsten do not propagate into the interface.



Keywords: divertor, tungsten-copper joint, FEM, cohesive zone model, delamination, crack propagation

DOI: 10.1585/pfr.20.1405018

## 1. Introduction

In developing conceptual designs of a fusion reactor, the divertor is expected for an important role as the exhaust of the He ash, which cannot be ignored for the continuous reaction in terms of controlling the atmospheric purity [1, 2]. However, exhaust process can cause so high heat flux to the surface of the divertor that its temperature would exceeds the melting point of materials without cooling. The divertor is therefore expected to remove heat system. In the divertor target of the Japanese DEMO, the copper chromium zirconium alloy (CuCrZr) is bonded as the pressurized water-cooling tubes with a copper (Cu) interlayer, and tungsten (W) is arranged to the surface because of its high melting point, thermal conductivity, and sputter resistance. However, it is estimated that the surface temperature reaches 1394°C at the maximum in a nominal operation [2]. This hot environment can yield large thermal stress, and cause crack initiation. Moreover, neutron irradiation may accelerate crack initiation and propagation. For the prediction of the total fracture assessment of the divertor, it is significant to figure out the elementary fracture process from the observation of flaws and numerical analyses.

Many studies have reported crack propagation in W during the heat loading test of a monoblock (MB) in the plasma-facing component, which covers the entire surface of the divertor [3–5]. Budaev *et al.* studied the W surface microstructure and found that the plural number of cracks was generated in recrystallized portions [6]. Panayotis *et al.* conducted a heat cycle analysis with the finite element method (FEM) and showed that the tensile stress near the surface exceeded the rupture strength of recrystallized W, which supports the crack initiation from the surface [7]. On the other hand, Richou *et al.* reported opened delamination on the W-Cu interface, connecting with a vertically propagated crack in W after thermal loading tests [8]. Plasma discharge operation conducted by Wang *et al.* also reported W-Cu delamination [9]. However, it is noted that the vertical W crack did not propagate into the interface during the operation. Although the geometry and heat conditions are not completely the same, i.e. number of heat cycles and inclination angle of the surface geometry [3–5, 6–8], this experimental result seems to have an indicative implication that the delamination could formerly have happened before the W vertical crack propagation started.

*Corresponding author's e-mail: tobata.yuta@qst.go.jp*

Since the delamination of the MB joint interface has a strong impact on the degradation of the cooling performance of W, the mechanism of this coupling fracture behavior should be elucidated and essentially requires a numerical evaluation method representing delamination behavior and its contact status such as stress or strain distribution.

As a candidacy for the evaluation, the cohesive zone model (CZM) is potentially useful for the prediction of the delamination behavior [10]. This method represents crack initiation and propagation behavior by defining kinetic interaction that represents stress relaxation in cohesive meshes as the inside interface of a crack. The interaction is called traction-separation law, which is expressed by the relationship between the apparent normal or shear stresses and the displacement of the cohesive meshes. Assuming a bilinear law, which is commonly used as traction-separation law (see Fig. 1) [11], the relation changes linearly until the applied stress reaches the maximum traction $\tau_{max}$. For higher displacement of the cohesive meshes, stress relaxation begins so that the stress decreases with an increase in their displacement. Because of the bilinear assumption, the traction-separation law can be expressed only by $\tau_{max}$ and the critical energy release rate $G_c$.

In previous studies, CZM has been used to predict the load-displacement relationship and to estimate $G_c$ by the double cantilever beam test [12–16] for the adhesive to the polymer composites or metal substrates. Mahler *et al.* also applied CZM analysis to the grain boundaries of multicrystal W. The analysis predicted the fracture load of the single-edge notch bending test and clarified the dependency of the fracture strength and the crack propagation direction on the grain geometry affected by the rolling press [17]. Wang *et al.* used CZM for representing grain fracture of tungsten microstructure around the top of the MB during cyclic heat loading [18]. However, this study did not consider the coupling kinetic effect of delamination on joint interface. A possible reason for this is the lack of experimental data at high temperatures regarding the interfacial mechanical properties of dissimilarly bonded materials. On the other hand, the utilization of the interface and bulk mechanical property data at room temperature may encourage useful parametric studies and provide a basic understanding of the delamination mechanism.

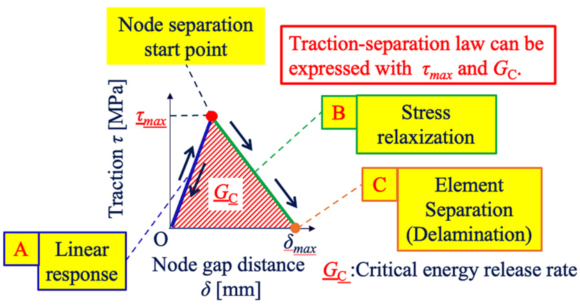


Fig. 1. Bilinear traction-separation law.

The objective of this study is to newly propose an evaluation method of the delamination mechanism of the MB utilizing CZM. In addition, this study aims to reveal the delamination process by the representation of the MB thermal loading test conducted with a simple testing geometry in a previous study [3]. For the compensation of the limited material data, parametric studies are conducted. Although there two dominant CZM parameters exist, we focus on the $\tau_{max}$ dependency of the delamination damage mechanism.

## 2. Numerical Analysis

### 2.1 Geometry and boundary condition

This study refers to an experiment of the cyclic thermal loading test conducted by Pintsuk *et al.* [3]. The study showed that a crack initiated and vertically propagated in the tungsten surface of the MB. However, the crack stopped and did not penetrate regardless of the multiple heat shots. It is noted that joint interface delamination was not mentioned, and its possibility remains unknown. Since the crack propagation may cause higher stress distribution around the interface due to the stress concentration of the crack tip, the delamination possibility needs to be elucidated. This is why, a finite element analysis model was created assuming that a crack propagation occurred after multiple cyclic heat loading, a slit shape notch was created with an equivalent length to the half thickness of the W surface region (Fig. 2). A commercial finite element analysis software, ANSYS mechanical 2023R1, was used. The model consists of 3091823 nodes and 1862903 isoparametric tetrahedra elements. A coordinate system was defined with X for the thickness direction, Y for the circumferential direction, and Z for the cooling water direction. Frictionless contact is applied to the interface of the notch between "a" and "c" regions in Fig. 2. A half-perpendicularly cut model to the central axis of the cooling pipe was considered. Frictionless support was set at the side planes of the model as continuous boundaries. The bottom plane of the monoblock is fixed. The inner surface of the CuCrZr alloy pipe was fixed at 120°C. The cooling water pressure was set at 3.3 MPa. Elasto-plastic analysis was performed. Plasticity was assumed to be bilinear, connecting the points of the yield strength and UTS. Temperature dependency of the mechanical and thermal material properties was considered. The material data is shown in Table 1 through Table 3 [19–71]. The heat load was linearly increased to 20 $MW/m^2$ in 1 s. The results of the thermal conduction analysis for each point of the W surface ("a"–"f") and the history of the temperature at the W-Cu interface are shown in Fig. 3. The temperature at the edge of the W surface showed the highest in the MB. Figure 3(b) shows the time-dependent temperature histories at points from "a" to "e" and the maximum temperatures at each point after 1 s of heating.

### 2.2 CZM

CZM was applied to the cohesive meshes of the W-Cu interface and the notch tip (between "c" and "f" in Fig. 2) for

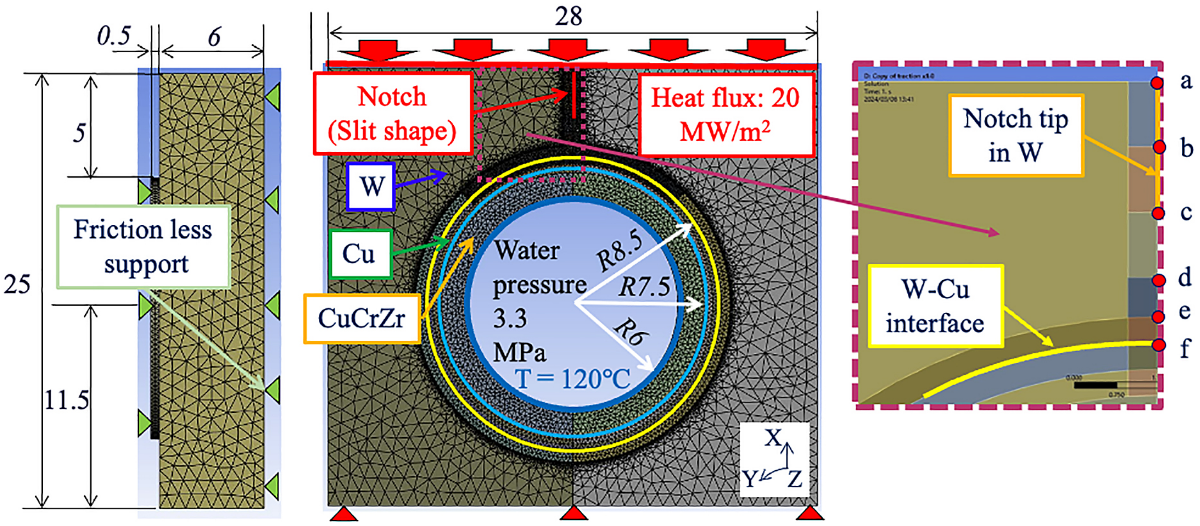


Fig. 2. FEM model.

Table 1. Input material data of tungsten [35, 37, 38, 49, 53, 55, 59–62].

| Temp. [°C] | Young's modulus [GPa] | Poisson's ratio [–] | True yield strength [MPa] | True strain at yield point [–] | True ultimate strength [MPa] | True total elongation Plastic strain [–] | Thermal expansion ratio [$\times 10^{-6}$/K] | Fracture Toughness [MPa/m$^{0.5}$] | Density [g/cm$^3$] | Thermal conductivity [W/mK] | Specific heat capacity [J/kgK] |
|---|---|---|---|---|---|---|---|---|---|---|---|
| 100 | 395 | 0.280 | 715 | 0.00180 | 818 | 0.148 | 4.40 | 8.69 | 19.3 | 156 | 140 |
| 200 | 394 | 0.281 | 635 | 0.00161 | 723 | 0.298 | 4.41 | 9.60 | 19.3 | 149 | 141 |
| 300 | 392 | 0.281 | 571 | 0.00145 | 706 | 0.391 | 4.42 | 11.1 | 19.2 | 143 | 142 |
| 400 | 389 | 0.282 | 520 | 0.00133 | 680 | 0.428 | 4.44 | 13.2 | 19.2 | 138 | 143 |
| 500 | 386 | 0.283 | 479 | 0.00124 | 651 | 0.314 | 4.46 | 15.9 | 19.2 | 133 | 145 |
| 600 | 383 | 0.294 | 446 | 0.00116 | 622 | 0.379 | 4.52 | 19.2 | 19.2 | 129 | 146 |
| 700 | 378 | 0.295 | 418 | 0.00110 | 591 | 0.471 | 4.56 | 23.1 | 19.1 | 125 | 148 |
| 800 | 374 | 0.297 | 392 | 0.00105 | 560 | 0.592 | 4.60 | 27.6 | 19.1 | 122 | 149 |
| 900 | 369 | 0.298 | 366 | 0.00099 | 526 | 0.746 | 4.65 | 32.7 | 19.1 | 119 | 151 |
| 1000 | 363 | 0.290 | 336 | 0.00092 | 486 | 0.938 | 4.70 | - | 19.0 | 116 | 153 |
| 1100 | 356 | 0.291 | 300 | 0.00084 | 439 | 1.17 | 4.75 | - | 19.0 | 114 | 155 |
| 1200 | 349 | 0.293 | 255 | 0.00073 | 382 | 1.45 | 4.81 | - | 19.0 | 111 | 157 |
| 1300 | 342 | 0.295 | 199 | 0.00058 | 314 | 1.78 | 4.88 | - | 18.9 | 109 | 159 |
| 1400 | 334 | 0.297 | 129 | 0.00039 | 233 | 2.17 | 4.95 | - | 18.9 | 107 | 162 |
| 1500 | 325 | 0.299 | 50.2 | 0.0150 | 157 | 0.567 | 5.03 | - | 18.9 | 105 | 164 |
| 1600 | 316 | 0.301 | 44.9 | 0.0140 | 131 | 0.521 | 5.10 | - | 18.8 | 104 | 166 |
| 1700 | 307 | 0.303 | 40.3 | 0.0130 | 106 | 0.465 | 5.19 | - | 18.8 | 102 | 169 |
| 1800 | 296 | 0.305 | 36.3 | 0.0120 | 82.8 | 0.397 | 5.28 | - | 18.7 | 100 | 171 |
| 1900 | 286 | 0.308 | 33.0 | 0.0120 | 60.5 | 0.317 | 5.37 | - | 18.7 | 98.8 | 174 |
| 2000 | 274 | 0.310 | 30.3 | 0.0110 | 38.7 | 0.224 | 5.47 | - | 18.7 | 97.3 | 177 |

Table 2. Input material data of Cu interlayer [19–21, 23, 26–28, 32, 36, 40, 41, 44, 45, 47, 48, 50, 51, 55, 56, 58, 63–67, 71].

| Temp. [°C] | Young's modulus [GPa] | Poisson's ratio [–] | True yield strength [MPa] | True strain at yield point [–] | True ultimate strength [MPa] | True total elongation Plastic strain [–] | Thermal expansion ratio [$\times 10^{-6}$/K] | Fracture Toughness [MPa/m$^{0.5}$] | Density [g/cm$^3$] | Thermal conductivity [W/mK] | Specific heat capacity [J/kgK] |
|---|---|---|---|---|---|---|---|---|---|---|---|
| 0 | 117 | 0.344 | 58.4 | 0.000499 | 323 | 0.628 | 16.7 | 8.95 | 402 | 387 | 140 |
| 100 | 114 | 0.346 | 53.3 | 0.000467 | 267 | 0.547 | 17.2 | 8.90 | 395 | 394 | 141 |
| 200 | 110 | 0.349 | 48.1 | 0.000437 | 218 | 0.479 | 17.6 | 8.85 | 388 | 401 | 142 |
| 300 | 105 | 0.352 | 42.8 | 0.000408 | 175 | 0.425 | 17.9 | 8.80 | 381 | 410 | 143 |
| 400 | 98 | 0.355 | 37.5 | 0.000381 | 138 | 0.384 | 18.2 | 8.74 | 374 | 419 | 145 |
| 500 | 90 | 0.359 | 32.0 | 0.000353 | 105 | 0.356 | 18.5 | 8.68 | 367 | 430 | 146 |

Table 3. Input material data of CuCrZr cooling pipe [50, 52].

| Temp. [°C] | Young's modulus [GPa] | Poisson's ratio [–] | True yield strength [MPa] | True strain at yield point [–] | True ultimate strength [MPa] | True total elongation Plastic strain [–] | Thermal expansion ratio [$\times 10^{-6}$/K] | Fracture Toughness [MPa/m$^{0.5}$] | Density [g/cm$^3$] | Thermal conductivity [W/mK] | Specific heat capacity [J/kgK] |
|---|---|---|---|---|---|---|---|---|---|---|---|
| 0 | 128 | 0.32 | 290 | 0.00226 | 482 | 0.212 | 16.7 | 8.91 | 323 | 388 | 140 |
| 100 | 125 | 0.36 | 276 | 0.00220 | 446 | 0.161 | 17.2 | 8.86 | 307 | 398 | 141 |
| 200 | 121 | 0.40 | 256 | 0.00211 | 404 | 0.125 | 17.6 | 8.82 | 286 | 407 | 142 |
| 300 | 116 | 0.44 | 232 | 0.00199 | 357 | 0.103 | 18.0 | 8.77 | 262 | 417 | 143 |
| 400 | 110 | 0.48 | 201 | 0.00183 | 305 | 0.0960 | 18.2 | 8.72 | 236 | 427 | 145 |
| 500 | 103 | 0.52 | 166 | 0.00161 | 248 | 0.103 | 18.4 | 8.66 | 210 | 437 | 146 |

a

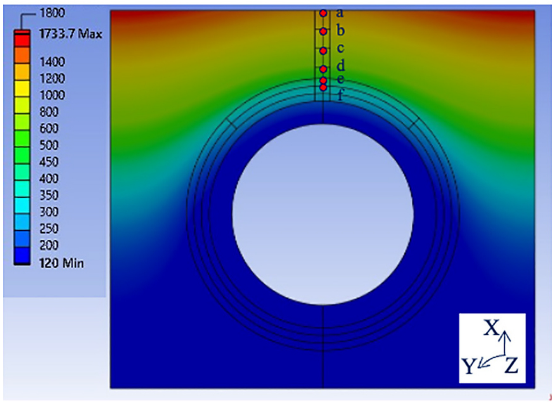


b

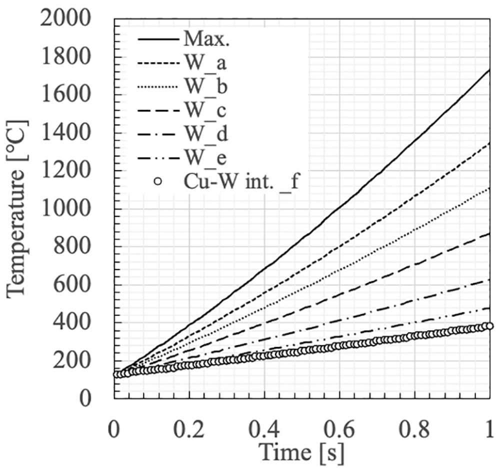


Fig. 3. Results of thermal conduction analysis. (a) Temperature distribution at $t = 1.0$ s. (b) Time history of temperature at point a–f.

the investigation of the combined behavior of crack propagation and delamination. We assume the bilinear traction-separation law (Fig. 1) [10]. Although there are no reports on CZM parameters, $\tau_{max}$, and $G_c$ of mode II, these parameters are generally larger than those of mode I [72, 73]. Hence, both parameters of mode II were assumed to be equivalent to those of mode I, for simplification in this study. Table 4 and Table 5 show the CZM parameters for the W-Cu interface and the W notch tip. Each parameter was defined considering the properties of the calculated maximum temperature of each section (Fig. 3(b)). The critical energy release rate Gc was calculated as follows.

Table 4. CZM parameters of W.

| Section | Ref. Temp. [°C] | CZM parameter $\tau_{I,\,max} = \tau_{II,\,max}$ [MPa] | CZM parameter $G_{Ic} = G_{IIc}$ [J/m$^2$] |
|---|---|---|---|
| e–f | 500 | 651 | 602 |
| d–e | 600 | 622 | 890 |
| c–d | 900 | 526 | 2700 |

Table 5. CZM parameters of W-Cu interface.

| No. | Ref. Temp. [°C] | CZM parameter $\tau_{I,\,max} = \tau_{II,\,max}$ [MPa] | CZM parameter $G_{Ic} = G_{IIc}$ [J/m$^2$] | CZM parameter $\delta_{I,\,max} = \delta_{II,\,max}$ [mm] |
|---|---|---|---|---|
| 1 | 400 | 34.5 | 100 | 0.00580 |
| 2 | | 52.4 | | 0.00381 |
| 3 | | 138 | | 0.00140 |

$$G_c = \left(1 - \upsilon^2\right)K^2/E, \tag{1}$$

where $v$ is Poisson's ratio, K is the fracture toughness, and E is Young's modulus. Since the bilinear law was assumed, $\delta_{max}$ was calculated by the following equation.

$$\delta_{max} = 2G_c/\tau_{max}. \tag{2}$$

Regarding $\tau_{max}$ of the joint interface, parametric studies were performed. Three cases of $\tau_{max}$ were defined. On the other hand, $G_c$ was fixed to the only case for excluding its dependency on the delamination mechanism.

## 3. Results

### 3.1 Interfacial normal stress

Figure 4 shows the time history of the normal stress on the W-Cu interface for each $\tau_{max}$. The left side of the image (OY) is located on the half-cut cross-section, or in the center of MB. On the opposite side, the edge of the interface is exposed to the surface. The blue area in the figure indicates compression. In the case of $\tau_{max}$ = 34.5 MPa, the interfacial normal stress was compression over time. This behavior was also observed for other $\tau_{max}$ cases.

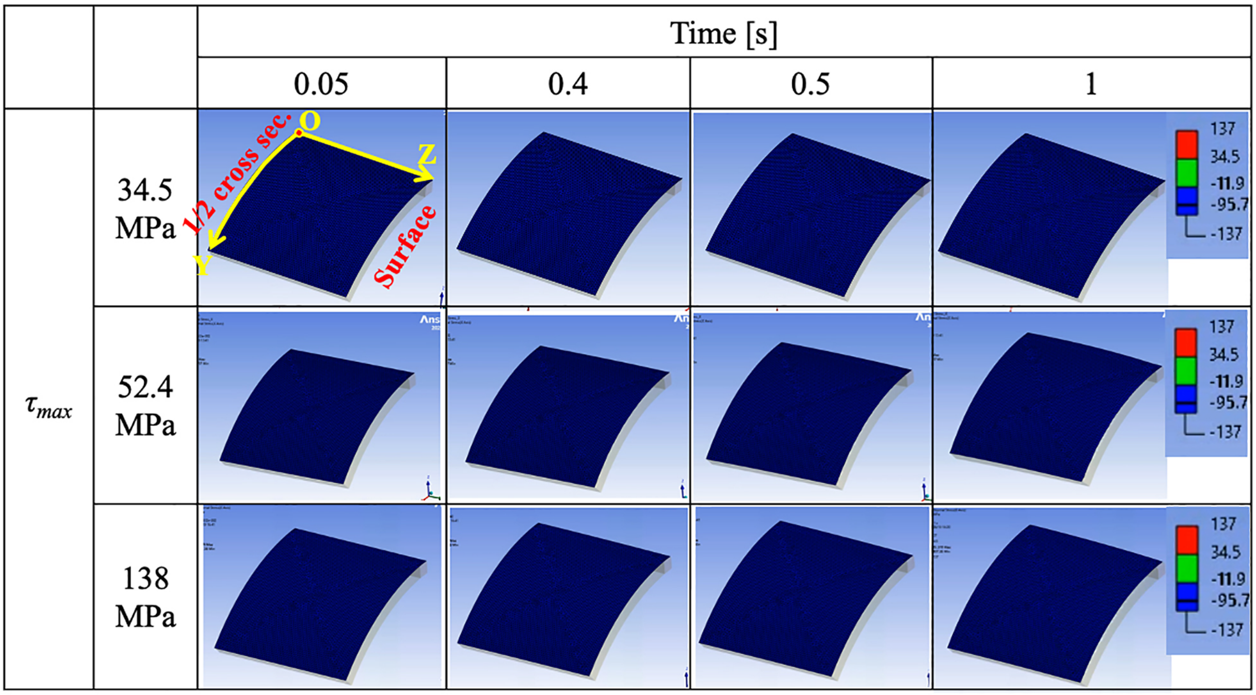


Fig. 4. Time history of interfacial normal stress of cohesive mesh at each $\tau_{max}$.

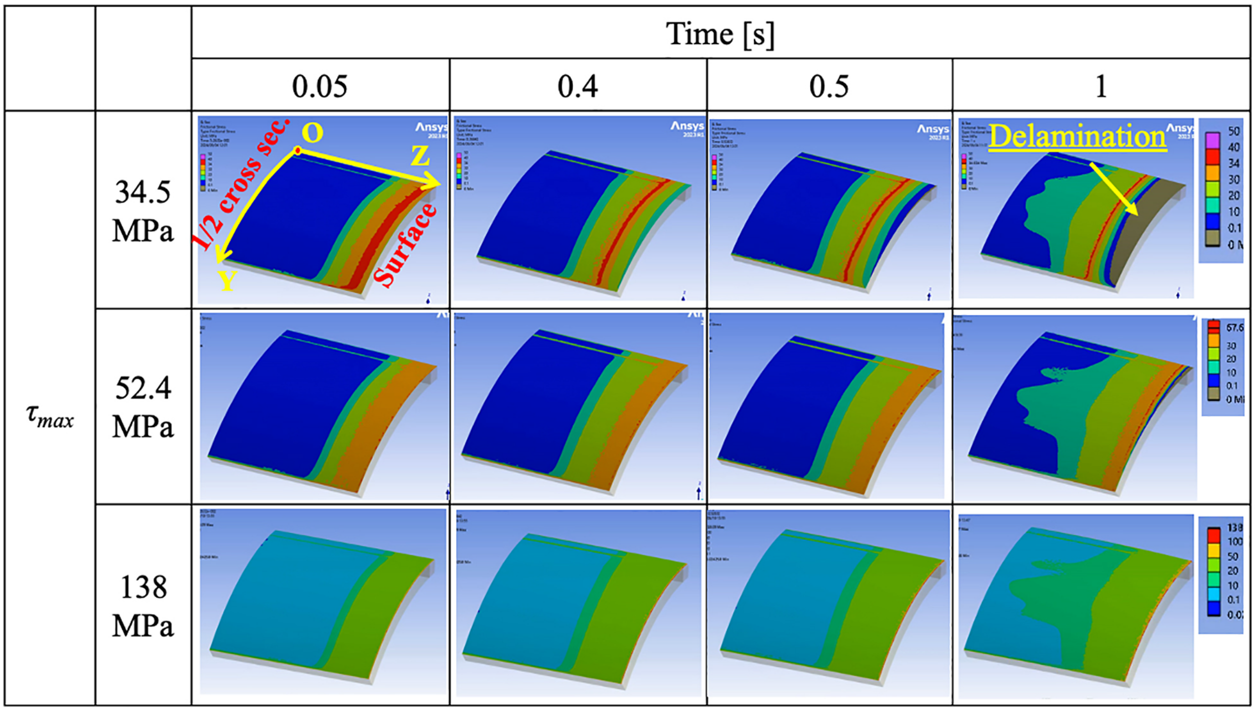


Fig. 5. Time history of interfacial shear stress of cohesive mesh at each $\tau_{max}$.

### 3.2 Interfacial shear stress

Figure 5 shows the time history of the combined shear stress $\tau_{XZ}$ and $\tau_{XY}$ (hereafter we call interfacial shear stress) at the W-Cu interface for each $\tau_{max}$. The left side of the red region shows the stress that exceeds $\tau_{max}$. In the case of $\tau_{max}$ = 34.5 MPa, the stress reached $\tau_{max}$ near the edge of the surface at t = 0.05 s. After that, the stress area moved toward OY. At t = 0.5 s, the region of the zero-shear stress appeared near the surface side. Then, at t = 1.0 s, this region expanded toward OY. In the case of $\tau_{max}$ = 52.4 MPa, a region exceeding $\tau_{max}$ was observed near the surface side at t = 0.05 s, as in the case of $\tau_{max}$ = 34.5 MPa. This region moved toward OY over time, too. In the case of $\tau_{max}$ = 138 MPa, a region exceeding $\tau_{max}$ was observed near the surface at t = 0.05 s. However, this region did not move with the lapse of time.

### 3.3 Interfacial displacement

Figure 6(a) shows the time series of the combined displacement with $\delta_{XZ}$ and $\delta_{XY}$ (hereafter we call interfacial shear displacement) on the W-Cu interface for each $\tau_{max}$. The left side of the image (OY) is located as well as Fig. 4. On the opposite side, the edge of the interface is exposed to the surface. In the case of $\tau_{max}$ = 34.5 MPa, the region above $\delta_{max}$ appeared at t = 0.5 s. At t = 1 s, the region expanded toward OY. In the case of $\tau_{max}$ = 52.4 MPa, the region that exceeds $\delta_{max}$ moved toward OY in 1.00 s as well. In the case of $\tau_{max}$ = 138 MPa, no region exceeds $\delta_{max}$.

Figure 6(b) shows the relationship between $\tau_{max}$ and the area fraction of the region exceeding $\delta_{max}$. The fraction means the ratio of the region above $\delta_{max}$ to the total surface area of the W-Cu interface. The graph shows that the case of $\tau_{max}$ = 34.5 MPa accounted for 14 % of the total area. On the other hand, in the case of $\tau_{max}$ = 52.4 MPa, the ratio drastically decreased to about 1%. In the case of $\tau_{max}$ = 138 MPa, the ratio was zero.

### 3.4 Stress distribution around the notch

Figure 7(a) shows the maximum normal stress in the Y direction near the notch tip (“c”–“d” region in Fig. 2). The plots show the numerical results for each $\tau_{max}$ case, and the broken line shows the UTS of W at the maximum temperature in the “c”–“d” region corresponding to each time. In the beginning, the stress increased rapidly with the increase of thermal loading but decreased as the time approached 0.4 s. Thereafter, however, the stress increased again. After 0.7 s, the stress stopped increasing. At all times, the stresses did not

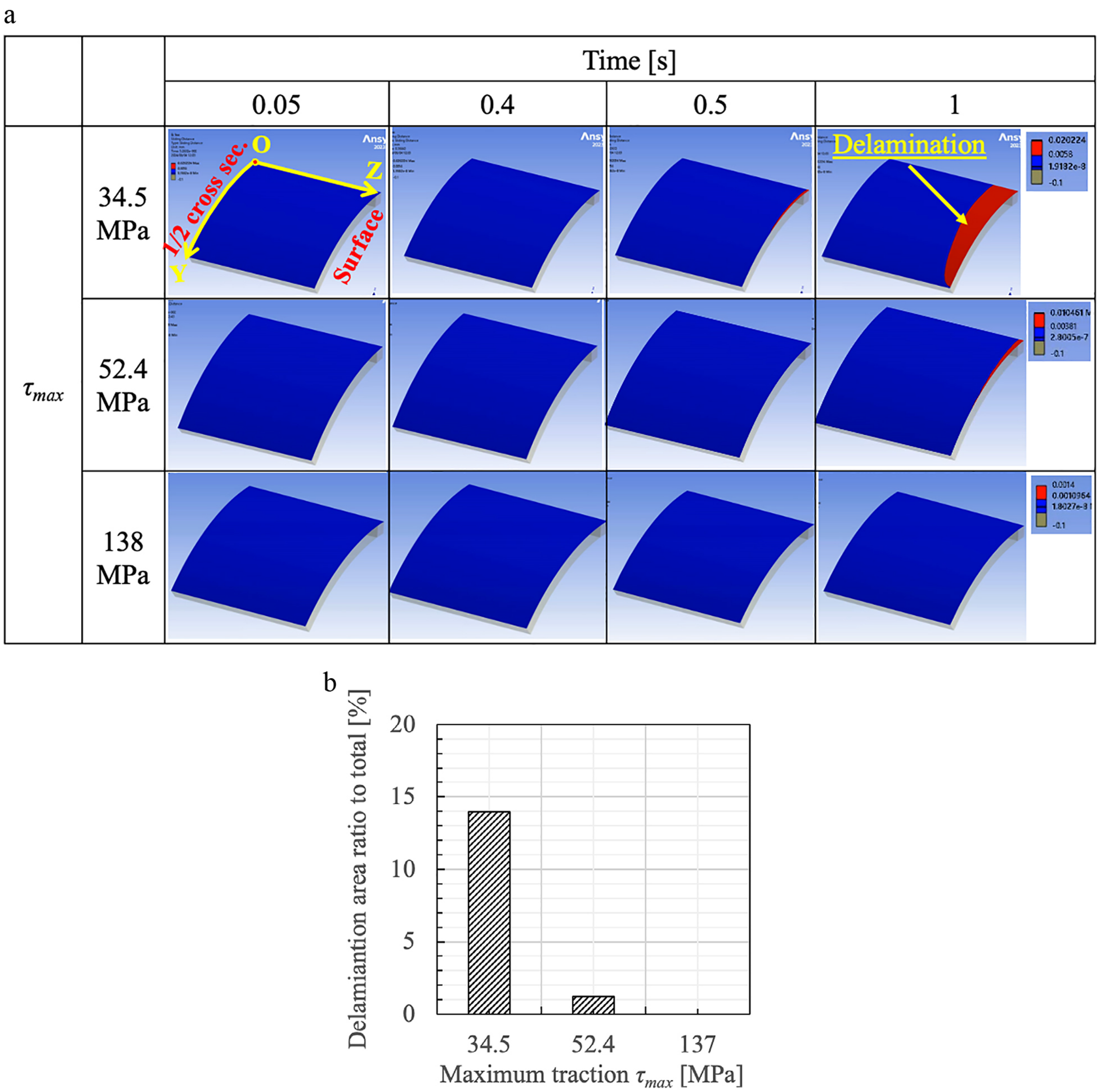


Fig. 6. Interfacial shear displacement behavior of cohesive mesh. (a) Time history of interfacial shear displacement of cohesive mesh at each $\tau_{max}$. (b) Area ratio of each $\tau_{max}$ where interfacial shear displacement exceeds $\delta_{max}$.

exceed $\tau_{max}$. Similar trends were observed for the other cases of $\tau_{max}$.

Figure 7(b) shows a typical ($\tau_{max}$ = 34.5 MPa) normal stress distribution in the Y direction near the notch tip of W ("c"–"d" region in Fig. 2). The left edge lies on the surface side, while the right edge lies in the center of MB. The red line in the figure indicates the notch tip. The blue area indicates compression. At t = 0.05 s, there was a uniform distribution of the high tensile stress region in the Z direction confirmed near the notch. However, the stress in this region decreased with time, and the area near the surface showed compression. On the other hand, from t = 0.7 to 0.9 s, the high tensile stress region expanded up from the bottom.

Figure 7(c) shows a typical ($\tau_{max}$ = 34.5 MPa) normal stress distribution on the surface side regarding the Y direction. The red line represents the notch. The yellow curve represents the W-Cu interface. The blue region indicates compression. The figure shows that at t = 0.05 s, a high tensile stress region was observed near the notch in Fig. 7(b). However, at t = 0.2 s, the region above the notch showed compression and sustained its downside expansion after t = 0.7 s. In contrast, the high tensile stress region emerged and moved toward the upside from the W-Cu interface.

## 4. Discussion

### 4.1 Delamination mechanism

As shown in Fig. 4, the interfacial normal stress showed compression. This indicates that there is no possibility of debonding due to mode I. On the other hand, as shown in Fig. 5 and Fig. 6(a), the regions where the interfacial shear stress exceeded $\tau_{max}$ but subsequently reached 0 corresponded to the regions where the interfacial stress exceeded $\delta_{max}$. This trend seems to result from the traction-separation law shown in Fig. 1. Therefore, it is suggested that mode II is a dominant delamination mode on the W-Cu interface.

We discuss $\tau_{max}$ dependency of the delamination mechanism as mentioned above by comparing the delamination process of each case of $\tau_{max}$ (34.5 MPa and 52.4 MPa) where the interface delaminated. In both cases, mode II was the dominant factor of the delamination. The delaminated region appeared near the surface side and headed for the center. This tendency was also reported in non-destructive testing with ultrasonic testing conducted by Wang *et al.* [9]. It also progressed toward the center side as well. Therefore, these tendencies seem to be independent of $\tau_{max}$. On the other hand, as

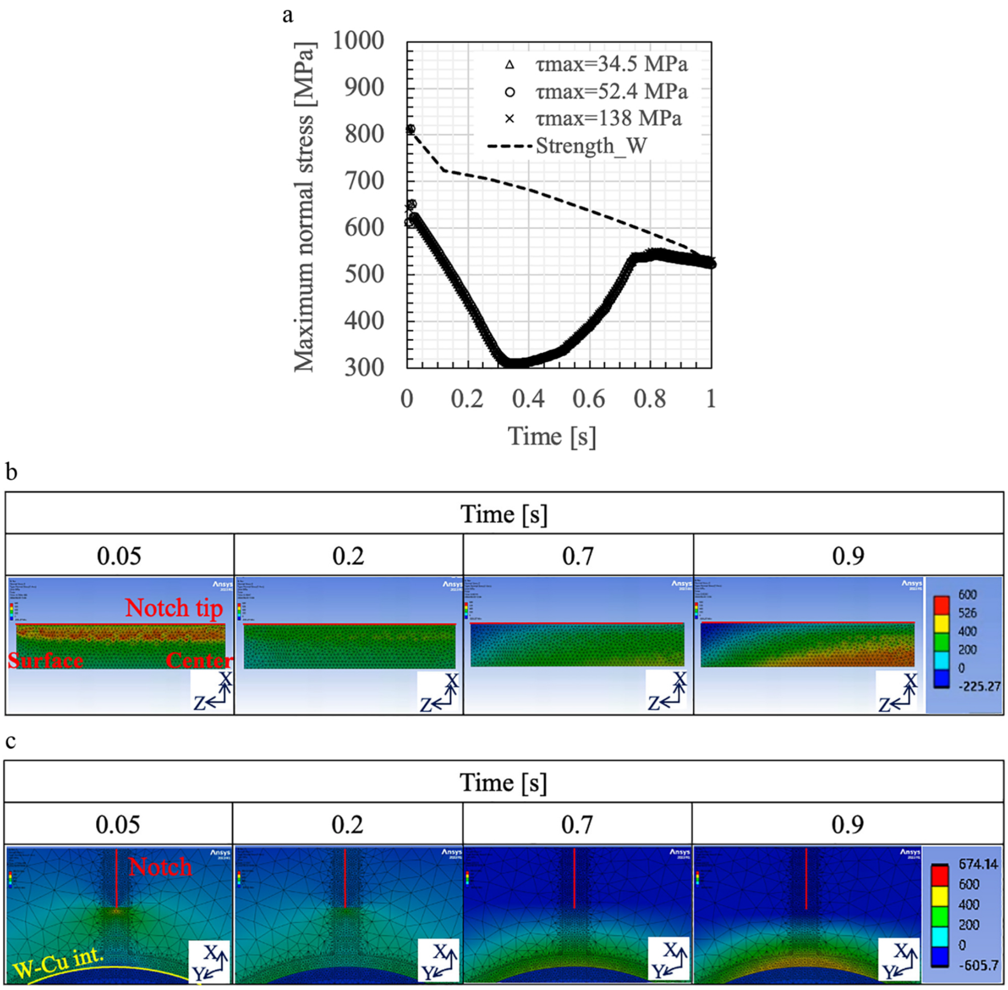


Fig. 7. Representative time history of interfacial normal stress at each $\tau_{max}$. (a) Time history of normal stress $\sigma_{YY}$ around notch tip (c–d region). (b) Normal stress $\sigma_{YY}$ distribution around notch tip ("c"–"d" region in Fig. 2). (c) Normal stress $\sigma_{YY}$ distribution around the surface.

shown in Fig. 6(b), the area beyond $\delta_{max}$ decreased with increasing $\tau_{max}$. Consequently, the delamination area seems to strongly depend on $\tau_{max}$.

### 4.2 Relationship between crack propagation and delamination

As shown in Fig. 7(a), until t = 0.4 s, the maximum normal stress in the Y direction of the "c"–"d" region decreased. One possible reason for this is that the compression was dominant around the notch because of the thermal expansion. On the other hand, from t = 0.4 to 0.7 s, the maximum normal tensile stress increased. This tendency seems to result from the growth of the thermal stress near the interface until t = 0.4 s. After t = 0.7 s, the maximum normal stress did not change and showed about 540 MPa. Meanwhile, the interface temperature at this time is 470°C, as shown in Fig. 3(b). The yield strength at this temperature is less than 520 MPa [50, 54, 55, 63]. This value is lower than the maximum normal stress. Therefore, the reason for the plateau after t = 0.7 s seems to be the yield of W.

Considering these normal stress variation processes, the vertical W crack propagation does not seem to occur. Nevertheless, as discussed in Sec. 4.1, the delamination possibly happens. This tendency has accordance with the experimental results of plasma discharge conducted by Wang *et al.* [9], which also supports the usefulness of applying CZM. Therefore, it is suggested that W-Cu interface delamination does possibly happen without vertical crack propagation in W.

### 4.3 Effect on the cooling capability

As discussed in Sec. 4.1, it is suggested that mode II is the dominant delamination factor. However, as shown in Fig. 4, the interface showed compression or contact. This result seems to be reasonable since the coefficient of thermal expansion of Cu is higher than that of W. Therefore, it is suggested that the cooling performance does not degrade regardless of the delamination during the heating process. However, a previous study reported that after thermal loading, a crack in the W section penetrated the W-Cu interface and opened [8]. Provided this situation, the interface may not be in contact, which can cause degradation of the cooling performance.

The current analysis only considers the process of the one heat shot, provided that cyclic heat loading had already been conducted and caused half depth vertical crack in W. However, this assumption fails to represent transient temperature and inelastic deformation history after multiple shots, comparing to real experiments. Therefore, it is necessary to numerically investigate the accumulative damage process in cyclic heat loading by utilizing the proposed numerical approach. In addition, inhomogeneous temperature distribution on the surface of the CuCrZr cooling pipe may have affection on the stress distribution around crack tip and W-Cu joint interface, and requires further investigation on its dependency.

### 4.4 CZM parameter

The effectiveness of the CZM parameters used in this analysis is discussed. The value of 138 MPa set as the one of $\tau_{max}$ conditions in this study is equal to the UTS of Cu at the maximum interface temperature during thermal loading (400°C) [65, 66]. However, the strength of the W-Cu joint was about 38% of that of Cu reported by Zhang *et al.* [74, 75], which means an apparent gap in the strength. Therefore, the numerical results substituting the CZM parameter seems to be unrealistic. Regarding $\tau_{max}$ = 52.4 MPa, the value is equivalent to 38% of the UTS of Cu and seems to be realistic. Moreover, $\tau_{max}$ = 34.5 MPa is closer to the lower limit of the dispersion referred from the previous studies [74, 75], which can be indicative in terms of the engineering design of the MB. Although this study ignores the temperature dependency of $\tau_{max}$ before reaching the maximum heat flux and may fail to predict the precise initiation time and area of the interface delamination, the debonding mechanism presented in this study does not depend on $\tau_{max}$ as mentioned in Sec. 4.1. Consequently, the qualitative trend predicted by the numerical results substituting 34.5 MPa and 52.4 MPa still seems to be realistic, which supports the usefulness of the CZM analysis.

The $G_c$ used in this study was 0.1 kJ/m$^2$. This value is too small compared to the value ($G_c$: 69.6 kJ/m$^2$) calculated from Eq. (1) by referring to the fracture toughness reported in a previous study [74]. Therefore, it is necessary to verify the $G_c$ dependency for accurate delamination behavior.

## 5. Conclusions

This study newly investigated the delamination mechanism between the tungsten and copper interlayer of the divertor monoblock under monotonic heat loading through the parametric study of the maximum traction $\tau_{max}$ by the finite element analysis applying CZM.

The proposed parametric study approach suggests delamination mechanism. In some cases of $\tau_{max}$, similar delamination behavior was confirmed to that reported by Wang *et al.* as follows; delamination in the W-Cu interface seems to happen before the vertical W cracks propagated into the interface, and to start from the surface side on the interface, heading for the center. Besides, it can be also noted that CZM has a desirable potential as a useful numerical tool for the evaluation of the joint delamination mechanism. By contrast, the interface keeps in contact because of the compression. This denies the possibility of the mode I delamination. Therefore, it is also proposed that mode II is a dominant factor of the delamination. In spite that the delamination can happen, however, degradation of the cooling capability does not seem to occur because of the closed interface during heating.

In this study, the dependency of $G_c$ remains ignored as well as that of temperature regarding $\tau_{max}$. These issues should be investigated in future works. Moreover, the effects of the cyclic heat and cooling process, tungsten crack penetration and inhomogeneous temperature distribution on the surface of cooling pipe may cause different fracture mechanisms and require further investigation.

## Acknowledgments

The authors appreciate attentive technical advice in multiple aspects regarding the model construction and its potential validity from Prof. Hisashi Serizawa, Dr. Wenhai Guan, and Mr. Chunyu He.

[1] K. Hoshino *et al.*, Plasma Fusion Res. **12**, 1405023 (2017).
[2] N. Asakura *et al.*, Nucl. Fusion **61**, 126057 (2021).
[3] G. Pintsuk *et al.*, Fusion Eng. Des. **88**, 1858 (2013).
[4] S. Nogami *et al.*, Fusion Eng. Des. **120**, 49 (2017).
[5] M. Fukuda *et al.*, J. Nucl. Mater. **542**, 152509 (2020).
[6] V.P. Budaev *et al.*, J. Nucl. Mater. **463**, 237 (2015).
[7] S. Panayotis *et al.*, Fusion Eng. Des. **125**, 256 (2017).
[8] M. Richou *et al.*, Fusion Eng. Des. **157**, 111610 (2020).
[9] Y. Wang *et al.*, Nucl. Mater. Energy **39**, 101665 (2024).
[10] X.-P. Xu and A. Needleman, J. Mech. Phys. Solids **42**, 1397 (1994).
[11] G. Alfano and M.A. Crisfield, Int. J. Numer. Methods Eng. **50**, 1701 (2001).
[12] X. Huo *et al.*, Int. J. Mech. Sci. **215**, 106921 (2022).
[13] M. Ma *et al.*, Heliyon **8**, e11037 (2022).
[14] J. Teixeira *et al.*, J. Adhes. **94**, 951 (2018).
[15] Y. Tobata *et al.*, Polym. Compos. **44**, 954 (2023).
[16] Y. Tobata *et al.*, J. Compos. Mater. **58**, 317 (2024).
[17] M. Mahler *et al.*, J. Nucl. Mater. **502**, 213 (2018).
[18] Y. Wang *et al.*, J. Nucl. Mater. **583**, 154555 (2023).
[19] A. Buch, *Pure metals properties* (ASM International, Ohio, 1999) p. 16.
[20] A. Buch, *Pure metals properties* (ASM International, Ohio, 1999) p. 34.
[21] A.P. Smirjagin *et al.*, *Industrial non-ferrous metals and alloys* (Metallurgy, Moscow, 1974) p. 29.
[22] ASME, Edition 2001 Section II, Part D - Properties, Table TM-3, 674 (2001).
[23] ASME, Edition 2001 Section II, Part D - Properties, Subpart 2, Physical Properties Tables, TABLE NF-1, 677 (2001).
[24] A.P. Smirjagin *et al.*, *Industrial non-ferrous metals and alloys* (Metallurgy, Moscow, 1974) p. 31–32.
[25] ASME, Edition 2001 Section II, Part D - Properties, Table NF-2, 678 (2001).
[26] ASME, Edition 2010 Section II, Part D - Properties (metric), Table TE-3, 715 (2010).
[27] ASME, Edition 2001, Section II, Part D - Properties, Subpart 2, Physical Properties Tables, TABLE NF-2, 678 (2001).
[28] B.N. Singh *et al.*, *Risø-R-1009*(EN) (Risø National Laboratory, Roskilde, 1998).
[29] B.N. Singh *et al.*, *Risø-R-839*(EN) (Risø National Laboratory, Roskilde, 1995).
[30] B.N. Singh *et al.*, *Risø-R-937*(EN). *Thermal Cycles, ITER R&D Task T213EU* (Risø National Laboratory, Roskilde, 1997).
[31] B.N. Singh *et al.*, *Risø-R-971*(EN) (Risø National Laboratory, Roskilde, 1997).
[32] B.N. Singh and S.J. Zinkle, J. Nucl. Mater. **206**, 212 (1993).
[33] C.R. Barrett and O.D. Sherby, Trans. AIME **230**, 1322 (1964).
[34] C. Yin *et al.*, Int. J. Refract. Metals Hard Mater. **75**, 153 (2018).
[35] C. Petersen and A. von der Weth, Final Report for Task: TW3-TTMA-002, Del 3, KIT (2010).
[36] C. Upthegrove and H.L. Burghoff, ASTM Special Technical Publication 181 (1956).
[37] C.Y. Ho *et al.*, J. Phys. Chem. Ref. Data **3**, 242 (1974).
[38] D. Rupp and S.M. Weygand, J. Nucl. Mater. **417**, 477 (2011).
[39] D.T. Hurd, *"Tungsten," Metals Handbook, Volume 1, Properties and Selection of Metals* (American Society for Metals, Ohio, 1961) p. 1225.
[40] Deutsches Kupferinstitut, Werkstoff - Datenblätter: Cu-OFE, Cu-DHP, Cu-ETP, Cu-HCP (2005).
[41] D.R. Lide and H.V. Kehiaian, *CRC handbook of thermophysical and thermochemical data* (CRC Press, Boca Raton, FL, 1994) p. 28.
[42] D.R. Lide and H.V. Kehiaian, *CRC handbook of thermophysical and thermochemical data* (CRC Press, Boca Raton, FL, 1994) p. 182.
[43] EN 1652:1997 + AC:2003, Copper and copper alloys – Plate, Sheet, Strip and Circles for General Purposes.
[44] S.A. Fabritsiev and A.S. Pokrovsky, J. Nucl. Mater. **249**, 239 (1997).
[45] G. Simmons and H. Wang, *Single Crystal Elastic Constants and Calculated Aggregate properties: A Handbook* (MIT Press, Cambridge, MA, 1971) p. 181.
[46] G.K. White and S.J. Collocott, J. Phys. Chem. Ref. Data **13**, 1251 (1984).
[47] H.M. Ledbetter and S.A. Kim, Mater. Sci. Eng. A, **101**, 87 (1988).
[48] H. Iida, Transmutation in Cu and Cu alloy, ITER report NAG-247 Cu Trans, N 73 RI 05-04-04 W 0.1, rev. 26 April, (Cu104) (2005).
[49] I.V. Gorynin *et al.*, J. Nucl. Mater. **191**, 421 (1992).
[50] ITER Document No. G74 MA16, ITER Material Properties Handbook, File Code: ITER-AK02-3112.
[51] J.R. Davis, *Copper and Copper Alloys, ASM Specialty Handbook* (ASM International, Ohio, 2001).
[52] K. Zhang *et al.*, Fusion Eng. Des. **144**, 148 (2019).
[53] M. Wirtz *et al.*, Phys. Scr. T **167**, 014015 (2016).
[54] M. Wirtz *et al.*, Nucl. Fusion **57**, 066018 (2017).
[55] M. Levy *et al.*, *Handbook of Elastic Properties of Solids, Liquids, and Gases, Vol. II*, (Academic Press, New York, 2001) p. 99, 340.
[56] M. Levy *et al.*, *Handbook of Elastic Properties of Solids, Liquids, and Gases, Vol. II* (Academic Press, New York, 2001) p. 99.
[57] M.W. Chase Jr., *NIST-JANAF Thermochemical Tables, 4th Ed.* (American Chemical Society and American Institute of Physics, New York, 1998), Vol. II, Cr-Zr, p. 1005.
[58] N.J. Simon *et al.*, *NIST Monograph 177* (National Institute of Standards and Technology, Washington DC, 1992).
[59] Nuclear fusion programme annual report of the Association Forschungszentrum Karlsruhe/EURATOM, January 2007 - December 2007, Programm Kernfusion, Forschungszentrum Karlsruhe, Wissenschaftliche Berichte, FZKA 7383.
[60] Plansee, "Tungsten", www.plansee.com, 2016. https://www.plansee.com/en/materials/tungsten.html
[61] R. Lowrie and A.M. Gonas, J. Appl. Phys. **28**, 4505 (1967).
[62] *Report on the Mechanical and Thermal Properties of Tungsten and TZM Sheet Produced in the Refractory Metal Sheet Rolling Program, Part 1* (Southern Research Institute, Alabama, 1966) p. 49–52.
[63] R.P. Reed and R.P. Mikesell, *NBS Monograph 101* (National Bureau of Standards, Washington DC, 1967).
[64] S.A. Fabritsiev and A.S. Pokrovsky, Intermediate report on Task G 74 TD 05 FR. October (2004).
[65] Specification for copper bar, bus bar, rod, and shapes, ASTM B187-94.
[66] W. Vandermeulen, Report FT/Mol/MAT-7/T85-003 (1985).
[67] Y.S. Touloukian, editor, (IFI/Plenum, New York-Washington, 1975) p. 77.
[68] Y.S. Touloukian and E.H. Buyco, *Thermophysical Properties of Matter, 4: Specific Heat, Metallic Elements and Alloys* (Plenum,

New York, 1970) p. 51–61.
[69] S.J. Zinkle, J. Phys. Metals Phys. **18**, 377 (1988).
[70] S.J. Zinkle and S.A. Fabritsiev, Supplement to Nuclear Fusion **5**, 163 (1994).
[71] A. Houhenwarter and R. Pippan, Mater. Sci. Eng. A **540**, 89 (2012).
[72] X.T. Miao *et al.*, Theor. Appl. Fract. Mech. **96**, 202 (2018).
[73] A. Pirondi and C.D. Donne, Eng. Fract. Mech. **68**, 1385 (2001).
[74] J. Zhang *et al.*, Mater. Des. **137**, 473 (2018).
[75] F. Li *et al.*, Metals **11**, 844 (2021).